

Motion Field Estimation from Alternate Exposure Images

Anita Sellent, Martin Eisemann, Bastian Goldlücke, Daniel Cremers and Marcus Magnor,

Abstract—Traditional optical flow algorithms rely on consecutive short-exposed images. In this work, we make use of an additional long-exposed image for motion field estimation. Long-exposed images integrate motion information directly in form of motion-blur. With this additional information more robust and accurate motion fields can be estimated. In addition the moment of occlusion can be determined. Considering the basic signal-theoretical problem in motion field estimation, we exploit the fact that long-exposed images integrate motion information to prevent temporal aliasing. A suitable image formation model relates the long-exposed image to preceding and succeeding short-exposed images in terms of dense 2D motion and per-pixel occlusion/disocclusion timings. Based on our image formation model, we describe a practical variational algorithm to estimate the motion field not only for visible image regions but also for regions getting occluded. Results for synthetic as well as real-world scenes demonstrate the validity of the approach.

Index Terms—Motion field estimation, motion blur, optical flow, occlusion, computational video.

I. INTRODUCTION

Estimating the dense motion field between two consecutive images has been a heavily investigated field of research for decades. Based on the classical optical flow equation most approaches require the numerical evaluation of the local time derivative. Hence, most optical flow algorithms work best with pinpoint-sharp images as input which depict a dynamic scene at two discrete points in time. If regarded individually, however, short-exposed images capture no motion information at all.

From sampling theory it is known that this approach leads to temporal aliasing if the maximum 2D displacement in the image plane exceeds one pixel [1]. To prevent aliasing, multiscale optical flow methods pre-filter the images globally in the spatial domain because the motion is a priori unknown [2]. This however is not the correct temporal filter: high spatial frequencies should be suppressed only in those Fourier-domain regions where aliasing actually occurs, i.e., only in the direction of local motion.

There exists a simple way to achieve correct temporal pre-filtering: exposing an image sensor for an extended period of time. For moving objects, high frequency components in motion direction are suppressed in long-exposed images. Apart from circumventing the problem of temporal aliasing, long-exposed images bear the advantage that occlusion enters into the image formation process. A scene point and its motion contribute to a motion-blurred image exactly for as long as the point is not occluded. Only recently have optical flow algorithms begun to address occlusion [3], [4], assigning occlusion labels per pixel. The moment of occlusion, however, cannot be easily determined from short-exposed images.

Inspired by these observations, we present an extension to traditional optical flow estimation. We obtain dense, robust 2D motion fields by using images with different exposure times of the same scene. As input, our method requires images taken such that an intermediate, long-exposed image I_B is enclosed by two short-exposed images I_1, I_2 , Fig. 1. In contrast to the severely underdetermined methods for motion estimation and image deblurring our approach, though still underdetermined, has more information available: The motion-blurred image provides anti-aliased motion information, while the short-exposed images provide complete high spatial frequencies.

Preliminary work on motion field estimation from alternate exposure images has appeared in [5], [6]. This journal version extends on earlier work to comprehensively present the complete method with in depth discussion of the signal-theoretical background in Sect. III and new supporting results on synthetic and real scenes.

II. RELATED WORK

The number of articles on optical flow computation is tremendous which indicates the significance of the problem as well as its severity [7]–[9]. Related to our work, scale-space approaches obtain reliable optical flow results in the presence of disparities larger than a few pixels [2], [10]. Alternatively, Lim et al. circumvent

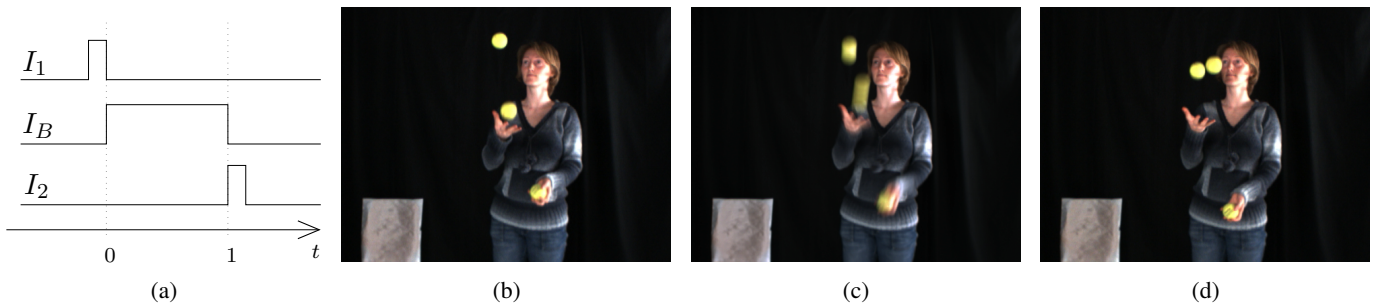


Fig. 1. Alternate exposure images: (a) exposure timing diagram of (b) a short-exposed image I_1 followed by (c) a long-exposed image I_B and (d) another short-exposed image I_2 .

the problem by employing high-speed camera recordings [11]. None of these approaches, however, consider occlusion. In contrast, Alvarez et al. determine occlusion masks by calculating forward and backward optical flow and checking for consistency [3]. Areas with large forward/backward optical flow discrepancies are considered occluded and are excluded from further computations. Xiao et al. propose interpolating motion into occluded areas from nearby regions by bilateral filtering [4]. This approach is refined by Sand and Teller [10] in the context of particle video. While explicit occlusion handling is incorporated, the moment of occlusion cannot be determined. The advantages of occlusion handling and occlusion timings for image interpolation are demonstrated by Mahajan *et al.* [12]. Similar to our approach they use a path-based image formation model. However, paths are calculated between two short-exposed images based on a discrete optimization framework yielding only full pixel accuracy.

There has been some previous work on calculating global motion from a single, motion-blurred image based on Fourier analysis [13] or auto-correlation [14] assuming spatially invariant motion. A recent approach [15] is able to calculate parametric and non-parametric motion fields by formulating a constraint on the alpha channel of the blurred image, shifting the problem to alpha-matte estimation. Motion estimation from a single motion-blurred image is part of blind image deblurring approaches. Because deconvolution is, in general, ill-posed, these approaches are restricted to spatially invariant point spread functions (PSF) [16]–[18] or a locally invariant PSF [19]. To simplify the problem of blind image deblurring, many approaches use additional images to estimate motion and to reconstruct the image: Yuan et al. [20] use pairs of blurred and noisy images not only to estimate a spatially invariant blur kernel but also to reduce ringing artifacts during deconvolution. The

hybrid camera of Ben-Esra and Nayar [21] takes a long-exposed image of the scene, while a detector with lower spatial and higher temporal resolution takes a sequence of short-exposed images to detect camera motion. From the camera motion, a global PSF is reconstructed which is used to deblur the image. A recent extension of the hybrid camera [22] permits the kernel to be a local mixture of predefined basis kernels, which can be handled by modern deblurring methods. The motion-from-smear approach [23] focuses on motion detection from two motion-blurred images, using deconvolution techniques and thus relying on locally constant motion. In an extension [24], a short-exposed and a long-exposed image are used to calculate the parameters of an affine motion model. The approach of Bar et al. [25] considers two motion-blurred images to segment an image into static background and a foreground that moves with constant velocity. Likewise, Agrawal et al. [26] determine a deblurred image from several blurred images with different exposure times. In a similar approach [27], at least two motion-blurred images are used to determine local motion, the corresponding segmentation and depth information of the scene, assuming motion to be a sideways translation parallel to the image plane.

In our approach we estimate dense motion fields from alternate exposure images directly without previous deblurring. The use of a motion-blurred image in combination with two short-exposed images allows us to calculate dense motion fields that are free to vary from pixel to pixel, i.e., the motion is not assumed to be globally constant, purely translational or affine nor does it assume any part of the scene to be static. In addition, our image formation model is able to handle occlusions as well as large displacements.

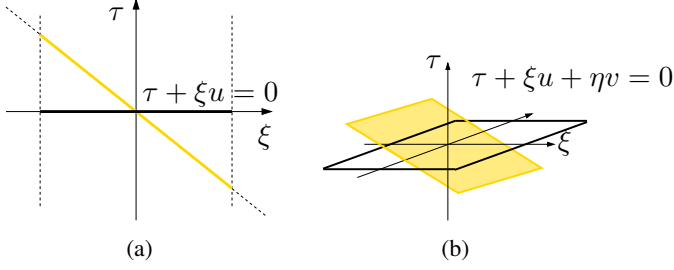


Fig. 2. (a) Static 1D or (b) 2D signals have space-time Fourier transforms with supports on the $(\tau = 0)$ hyperplane (black). Moving the signal uniformly shears the support to lie on the motion-dependent hyperplane $\tau + \xi u = 0$ or $\tau + \xi u + \eta v = 0$ respectively (gray/ yellow).

III. SIGNAL-THEORETIC MOTIVATION

From sampling theory it is well known that regularly sampling a signal at a frequency below its Nyquist limit leads to aliasing artifacts. In the case of 2D motion aliasing, this effect is also known as the *wagon-wheel-effect*.

To evaluate temporal aliasing and its consequences to motion estimation analytically, we assume the simple case of a band-limited, continuous image $f_0(x, y)$ that is moving with a uniform velocity $\vec{w} = \begin{pmatrix} u \\ v \end{pmatrix}$, i.e., $f(x, y, t) = f_0(x - ut, y - vt)$. The 3D Fourier transform $F(\xi, \eta, \tau)$ of the moving image is related to the 2D Fourier transform $F_0(\xi, \eta)$ of the static image via

$$\begin{aligned} F(\xi, \eta, \tau) &= \iiint f(x, y, t) e^{-2\pi i(\xi x + \eta y + \tau t)} dx dy dt \\ &= \iiint f_0(\tilde{x}, \tilde{y}) e^{-2\pi i(\xi \tilde{x} + \eta \tilde{y}) + 2\pi i t(\tau + \xi u + \eta v)} d\tilde{x} d\tilde{y} dt \\ &= F_0(\xi, \eta) \delta(\tau + \xi u + \eta v) \end{aligned}$$

where δ is the Dirac delta. While the support of F_0 is in the $(\tau = 0)$ -plane, the support of the space-time Fourier transform of the uniformly moving image is located on the hyperplane $\begin{pmatrix} u \\ v \end{pmatrix}^\perp$, i.e., the support is normal to the motion direction. Additionally, the support is stretched according to motion magnitude, Fig. 2.

Point-wise sampling leads to shifted replica of the original transform in the frequency domain at a distance inverse to the sampling distance. If the signal is moving, sampling in time can lead to aliasing even for spatially band-limited signals: Motion that is larger than the inverse of twice the spatial band-limit per frame shears the support of the 3D Fourier transform up to the point where the projections of the supports of the replica to the $(\xi = 0, \eta = 0)$ -plane overlap, Fig. 3.

For a fixed point (x_0, y_0) the temporal intensity func-

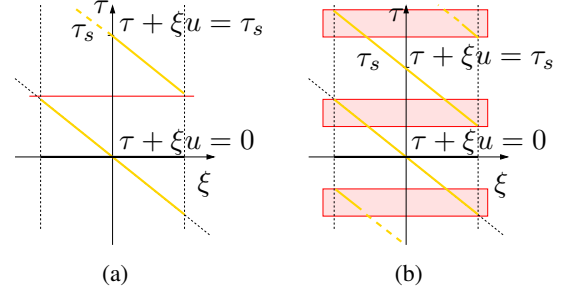


Fig. 3. Regular temporal sampling of a moving 1D signal with sampling frequency τ_s leads to replica in the space-time Fourier domain. (a) If motion is smaller than one pixel per frame, the projections of the replica to the τ axis don't overlap. (b) For larger motion the projections of the replica on the τ axis overlap (boxes) and therefore cause aliasing artifacts if used without adequate filtering.

tion $\phi(t) = f(x_0, y_0, t)$ has the Fourier transform

$$\begin{aligned} \Phi(\tau) &= \int \phi(t) e^{-2\pi i \tau t} dt \\ &= - \iint e^{2\pi i(\eta y_0 + \xi x_0)} F(\xi, \eta, \tau) d\xi d\eta \quad (2) \end{aligned}$$

which is derived in the Appendix. Eq. (2) shows that $\Phi(\tau)$ is a weighted projection of $F(\xi, \eta, \tau)$ to the $(\xi = 0, \eta = 0)$ -plane so that overlap of the replica due to fast motion introduces aliasing. As temporal derivatives transform to multiplication with $2\pi i \tau$ in the frequency domain, the overlap causes aliasing also when the temporal derivative for a fixed point is considered. Yet, temporal derivatives are used in all optical flow algorithms based on the color constancy assumption. The straight-forward approach to separate the replica is to (1) increase the sampling rate. High-speed cameras provide high temporal sampling rates, and the optical flow can be determined between consecutive images [11]. We compare the results of this approach to motion fields calculated on alternate exposure images in Sect. VI.

If no high-speed video equipment is available, other methods have to be applied to avoid aliasing at high spatial frequencies. In multiscale optical flow approaches, the entire image is low-pass filtered isotropically in both spatial directions, Fig. 4(a), to indiscriminately remove high spatial frequencies. While this approach does remove the frequencies that cause aliasing, it also destroys high frequency information that is not affected by aliasing at all and can be used to limit the solution space of the motion estimation problem.

A pre-filtering restricted to the direction in which aliasing actually occurs can be obtained by using longer exposure times. Approximating the shutter function with

the boxcar-function

$$h(x, y, t) = \begin{cases} 1 & \text{if } |t| \leq \frac{T}{2} \\ 0 & \text{else} \end{cases} \quad (3)$$

where T is the total duration of the exposure, a long exposed image $g(x, y, t) = (f * h)(x, y, t)$ has the 3D Fourier transform

$$\begin{aligned} G(\xi, \eta, \tau) &= \iiint_{-\frac{T}{2}}^{\frac{T}{2}} f(x, y, t + s) ds e^{-2\pi i(\xi x + \eta y + \tau t)} dx dy dt \\ &= F_0(\xi, \eta) T \text{sinc}(\pi T(\xi u + \eta v)) \delta(\tau + \xi u + \eta v) \end{aligned} \quad (4)$$

In consequence, the high frequencies of the original image are correctly low-pass filtered dependent on the motion, Fig. 4(b).

Though suited for considering temporal derivatives, the use of motion blurred images for other purposes, e.g. frame interpolation, is limited as high frequencies in motion direction are lost during recording and their reconstruction is an ill posed problem. In our approach we employ alternating short- and long-exposure images to record the high frequencies. We also derive an image formation model that relates short-exposure images via a long-exposure image and the desired motion and thus obtain motion information without temporal derivatives, i.e., a scale-space approach is no longer necessary to avoid aliasing but is only an option to speed up convergence.

IV. IMAGE FORMATION MODEL

In order to exploit the information provided by the additional long-time exposed image, we need an image formation model that relates the acquired images via a dense 2D motion field. As input, we assume two short exposure images $I_1, I_2 : \Omega \rightarrow \mathbb{R}$ which are taken before and after the exposure time of a third, long-exposed input

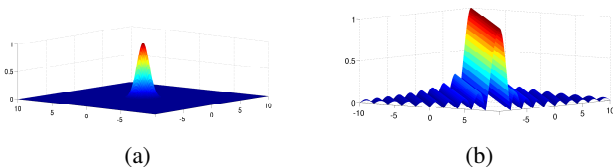


Fig. 4. (a) The isotropic spatial filter used in multiscale optical flow algorithms attenuates all high frequencies indiscriminately. (b) Long-exposure imaging corresponds to filtering the image with an anisotropic filter that attenuates high frequencies only in the direction where temporal aliasing occurs due to the underlying motion. Frequencies perpendicular to this direction are left unchanged.

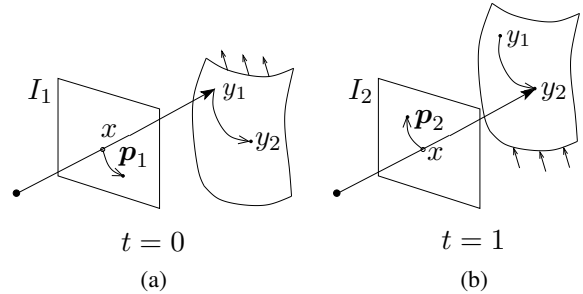


Fig. 5. Without occlusion, a contiguous path of moving scene surface points between y_1 and y_2 contributes to pixel x in the long-exposure image. (a) The projection of the path onto the image plane forms a planar curve p_1 in the preceding short-exposed image I_1 and (b) a planar curve p_2 in the succeeding short-exposed image I_2 .

image $B : \Omega \rightarrow \mathbb{R}$. We look for a description of B in terms of I_1, I_2 and the motion field.

Some additional assumptions are made. We assume that the short-exposed images are free of motion-blur and that short-exposed and long-exposed images are brightness-adjusted such that in case of no motion, all images are identical. In practice, we adjust the gain factor of the camera according to the exposure duration. Finally, we assume that scene surface appearance does not change considerably between the exposure time of all three images.

A. Without Occlusion

Our goal is to derive a suitable model for the formation of the motion-blurred image B , which is both computationally manageable as well as sufficiently accurate to describe real-world data. For the simplest case, let us consider a moving scene without any occluded or disoccluded scene points, which implies that all scene points contributing to the motion-blurred image B are visible in I_1 as well as I_2 . Parametrizing by time $t \in [0, 1]$ we obtain

$$B(x) = \int_0^1 I_1(p_1(x, t)) dt = \int_0^1 I_2(p_2(x, t)) dt. \quad (5)$$

where $p_1(x, \diamond) : [0, 1] \rightarrow \Omega$ and $p_2(x, \diamond) : [0, 1] \rightarrow \Omega$ are spatially varying, planar curves on the image plane with $p_1(x, 0) = x$ and $p_2(x, 0) = x$, Fig. 5. For each input image, the curves describe the points on the image plane which pass through x during the exposure duration. While p_1 orders the points forward in time, p_2 orders them backward in time. In the case without occlusion, the entire curves are visible in both images, so that the values of both integrals are equal.

B. With Occlusion

The long-exposed image enables incorporating occlusion effects into the image formation model. We assume that a point changes its visibility at most once during the exposure. If a scene surface becomes occluded, some parts of the motion paths are visible in only one of the two short-exposure images, Fig. 6. We partition the integral so that part of the intensity $B(x)$ observed in x is due to intensities along curve \mathbf{p}_1 , while the remaining part is due to intensities along \mathbf{p}_2 ,

$$B(x) = \int_0^{s(x)} I_1(\mathbf{p}_1(x, t)) dt + \int_0^{1-s(x)} I_2(\mathbf{p}_2(x, t)) dt. \quad (6)$$

Here, $s(x) \in [0, 1]$ denotes the moment during exposure where an object previously visible at position x in I_1 becomes occluded by an object visible at x in I_2 , or vice versa.

Note that in the case of no occlusion, any choice of s yields the same intensity $B(x)$. The occlusion timings are only well defined in areas where occlusion actually takes place. At all other points any value $s \in [0, 1]$ is equally valid. If we consider a fixed, non-occluded x and differentiate (6) with respect to s , we obtain the brightness constancy assumption of traditional optical flow computation by the fundamental theorem of calculus. Thus our approach is a generalized image formation model that incorporates the additional information provided by the motion-blurred image, and explicitly takes occlusion into account.

The image formation model can be easily extended to allow for more than one visibility change, given that all passing pixels are visible either in I_1 or I_2 . However, for the sake of stability of the algorithm, Sect. V, and

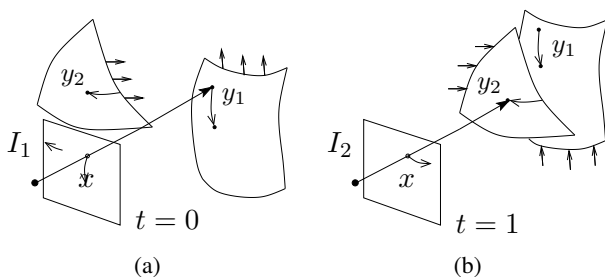


Fig. 6. With occlusion, the path of scene surface points contributing to pixel x in the long-exposure image is split into two parts. The first part is on the occluded, the second part is on the occluding surface. (a) The path has a non-contiguous projection to the image plane of the preceding image I_1 and (b) is only partly visible in the succeeding image I_2 .

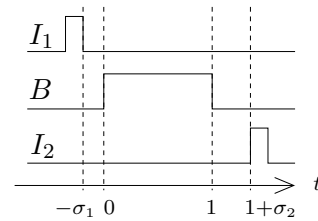


Fig. 7. We include a temporal offset to account for gaps that occur due to hardware constraints. For normalized exposure time of B the gap between I_1 and B has duration σ_1 and the gap between I_2 and B has duration σ_2

since multiple occlusions arise only rarely in practical situations with reasonable frame rates, we do not further investigate this extension here.

C. With Temporal Offset

We want to allow for exposure gaps between the images I_1 and B as well as between B and I_2 , Fig.7. Gaps between exposures occur, e.g., due to camera hardware constraints. Scene motion, of course, continues during such exposure gaps. To account for gaps, we include a temporal offset in (6) by changing the integration limits corresponding to the relative lengths of the gaps:

$$B(x) = \int_{\sigma_1}^{\sigma_1+s(x)} I_1(\mathbf{p}_1(x, t)) dt + \int_{\sigma_2}^{\sigma_2+1-s(x)} I_2(\mathbf{p}_2(x, t)) dt. \quad (7)$$

σ_1 is the quotient of the length of the exposure gap between I_1 and B and the exposure duration of B . Correspondingly, σ_2 is the quotient of the length of the exposure gap between B and I_2 and the exposure duration of B and as before $s(x) \in [0, 1]$ is the moment of occlusion.

Note that the motion curves \mathbf{p}_1 and \mathbf{p}_2 describe the motion in the coordinate frame of the motion-blurred image. Since for many applications a forward or backward motion field is needed, we morph the motion curves according to the estimated motion and occlusion parameters to obtain a motion field for I_1 and I_2 , respectively.

The image formation model described above gives rise to a minimization problem of an energy functional, which is derived in the next section. In the image formation model described so far, we used general motion curves. To simplify computations, we adopt here a linear motion model so that

$$\mathbf{p}_1(x, t) = x - t \mathbf{w}_1(x) \quad \text{and} \quad \mathbf{p}_2(x, t) = x + t \mathbf{w}_2(x), \quad (8)$$

where $\mathbf{w}_j : \Omega \rightarrow \mathbb{R}^2$, $\mathbf{w}_j(x) = \begin{pmatrix} w_{j,1}(x) \\ w_{j,2}(x) \end{pmatrix}$ for $j \in \{1, 2\}$. This turns out to be a suitable approximation also for more general types of motion, Sect. VI. If desired, however, it is straight-forward to extend the algorithm to more complex motion models.

D. Frame Interpolation

The image formation model can also be interpreted as a model for image interpolation for frames at intermediate time instants $t \in [0, 1]$

$$I_t(x) = \begin{cases} I_1(x - (t + \sigma_1)\mathbf{w}_1) & \text{if } t \leq s(x) \\ I_2(x + (t + \sigma_2)\mathbf{w}_2) & \text{if } t > s(x). \end{cases} \quad (9)$$

This model handles occlusion in an implicit way and does not necessitate any thresholding or special treatment of the occluded and disoccluded regions.

V. ENERGY FORMULATION

The image formation model for a motion-blurred image B considered in the previous section yields a pointwise error measure for estimates of the linear motion paths \mathbf{w}_1 , \mathbf{w}_2 and the occlusion time s as follows. Given two short-exposed images I_1 , I_2 and a long-exposed image I_B , i.e., the actual measurement, we can compare the blurred image I_B to the result B predicted by the model (7). We found the L^1 norm to be more robust than the L^2 norm [5] so we consider the differences between measurement and prediction in L^1 :

$$\rho_1(x, s(x), \mathbf{w}_1(x), \mathbf{w}_2(x)) = |I_B(x) - B(x)|. \quad (10)$$

For the sake of increased subpixel accuracy we also include the differentiated version, i.e., the brightness constancy assumption

$$\rho_2(x, s(x), \mathbf{w}_1(x), \mathbf{w}_2(x)) = |I_1(x - s\mathbf{w}_1) - I_2(x + (1 - s)\mathbf{w}_2)|. \quad (11)$$

Integrating the weighted sum of the pointwise errors over the image domain, we obtain the data term

$$E_{data}(s, \mathbf{w}_1, \mathbf{w}_2) = \int_{\Omega} \rho_1 + \gamma \rho_2 \, dx, \quad (12)$$

with $\gamma \geq 0$, cf. Sect. VI-C.

Instead of minimizing the pointwise error, we can increase stability and performance in textureless regions by considering global relationships of scene movement: Neighboring points belonging to the same object typically exhibit similar motion. This observation suggests including a regularization term in the energy functional. As demonstrated in previous work [28], using the total

variation as a regularizer for flow fields yields superior results. Total variation regularization favors piecewise constant motion fields. Thus it smoothes out undesired outliers and avoids oversmoothing at motion boundaries at the same time. We also regularize the occlusion time as neighboring pixels, if they are occluded at all, are occluded at related instants in time. The resulting energy which depends on the unknown motion \mathbf{w}_1 , \mathbf{w}_2 and occlusion time s can be written as

$$E = E_{data} + \int_{\Omega} \alpha \sum_{i=1}^2 (|\nabla w_{1,i}| + |\nabla w_{2,i}|) + \beta |\nabla s| \, dx. \quad (13)$$

Here, $\alpha, \beta \geq 0$ are free parameters of the approach that control the desired smoothness of the flow fields and of the moment of occlusion, respectively, cf. Sect. VI-C.

A. Minimization Method

Our minimization scheme is based on the primal-dual algorithm used for TV- L^1 optical flow [28], whose variants currently rank in the top of the Middlebury benchmark [29]. We briefly review the method here and show how we adopt the framework to minimize our more complex energy functional. In turn we replace the general variable with \mathbf{w}_1 , \mathbf{w}_2 and s and keep the others fixed.

For the very general case of minimizing a total variation energy of the form

$$E(\mathbf{u}) = \lambda \int_{\Omega} |\rho(\mathbf{u})| \, dx + \int_{\Omega} \sum_{i=1}^k |\nabla u_i| \, dx \quad (14)$$

for a k -dimensional function \mathbf{u} on Ω with a pointwise error term ρ , an auxiliary vector field \mathbf{v} is introduced and the approximation

$$E_{\theta}(\mathbf{u}, \mathbf{v}) = \int_{\Omega} \lambda |\rho(\mathbf{v})| + \frac{1}{2\theta} \|\mathbf{u} - \mathbf{v}\|^2 + \sum_{i=1}^k |\nabla u_i| \, dx \quad (15)$$

is considered instead. If θ is small, \mathbf{v} will be close to \mathbf{u} near the minimum, and thus E will be close to E_{θ} . The key result of Ref. [28] is that (15) can be minimized very efficiently using an alternating scheme that iterates between solving a TV image denoising problem for each u_i , keeping \mathbf{v} fixed

$$\operatorname{argmin}_{u_i} \int_{\Omega} \frac{1}{2\theta} (u_i - v_i)^2 + |\nabla u_i| \, dx, \quad (16)$$

and a minimization problem for \mathbf{v} with fixed \mathbf{u}

$$\operatorname{argmin}_{\mathbf{v}} \lambda |\rho(\mathbf{v})| + \frac{1}{2\theta} \|\mathbf{u} - \mathbf{v}\|^2, \quad (17)$$

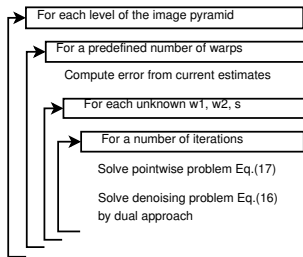


Fig. 8. Workflow of our algorithm.

which can be solved pointwise with a thresholding scheme. Details and proof of convergence can be found in Refs. [28], [30].

B. Application of the Minimization Method

In our case, we employ some small modifications adapted to our problem of minimizing the energy in terms of w_1 , w_2 and s . First, we employ the above scheme, i.e., iterating between (16) and (17), by considering $u = w_1$, $u = w_2$ or $u = s$, respectively, to solve for each of the unknowns given a fixed approximation of the others. As the thresholding scheme of Ref. [28] is not directly applicable to our non-linear data term we apply a descent scheme for (17), substituting the L^1 norm with its regularized variant $|\rho_i|_\epsilon = \sqrt{|\rho_i|^2 + \epsilon}$. We set $\epsilon = 0.001$ throughout all experiments.

C. Implementation

The numerical techniques for the actual minimization are well known [28].

In order to speed up convergence, we implemented the algorithm on a scale pyramid of factor 0.5 initializing with $s = 0.5$ for the occlusion timing, and $w_1, w_2 = 0$ on the coarsest level. On each level of the pyramid we perform several warping iterations where in each iteration we solve for s , w_1 and w_2 . For each variable an instance of (16) and (17) has to be solved, Fig. 8.

For (16), we employ the dual formulation detailed in Ref. [28], Proposition 1, using 5 iterations and a time step of 0.1225.

For all experimental results we use a 5-level image pyramid, 10 warping iterations and 10 iterations to solve (16) and (17). Suitable values for the parameter α , β , γ and θ were found experimentally. For normalized intensity values we found $\theta \in (0, 1]$, $\alpha, \beta \in (0, 0.1]$ and $\gamma \in [0, 0.5]$ to be suitable value ranges. A discussion of the sensitivity on the parameter choice is given in Sect. VI.

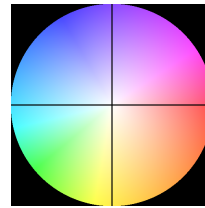


Fig. 9. The color map used to display motion fields in Fig. 11, 14, 15 and 16.

We implemented the algorithm in MATLAB. With code optimized for readability and not for speed the estimation of a 225×320 pixel motion field on a 3.06 GHz processor lasts 191s. As the process is highly parallel, a GPU implementation to speed up the computation is possible.

VI. EXPERIMENTS AND EVALUATION

To evaluate TV- L^1 motion field estimation from alternate exposure images we consider synthetic test data as well as real-world recordings. For synthetic scenes with known ground-truth motion fields we calculate motion fields with our algorithm as well as with related approaches [5], [10], [11], [28] and compare the mean angular error (MAE) and the mean endpoint error (MEE). We interpolate intermediate frames using estimated motion fields and occlusion timings and compare them to ground-truth images, images interpolated with ground-truth motion and images interpolated with optical flow. Note that we cannot evaluate our method on standard test data because these test sets do not provide any motion-blurred images I_B . We also show results for real world recordings. The recordings were made with a PointGrey Flea2 camera that is able to acquire short and long-exposed images alternately. For visualization of the motion fields we use the color map in Fig. 9 together with a sparse overlay of the motion vectors which are scaled for better visualization.

We use image interpolation with our image formation model (9) as means to evaluate the calculated occlusion timings. Occlusion timings can have arbitrary values $s \in [0, 1]$ at non-occluded points and are therefore hard to evaluate visually. Fig. 10 shows examples of the estimated occlusions timings color-coded with $s = 0$ as black and $s = 1$ as white. Changes of s as the transition from black to white at the wings of the windmill, Fig. 10(a), are hard to spot in the otherwise arbitrary variation of s . In contrast, erroneous occlusion timings in regions where occlusion actually occurs are easily visible in interpolated images, Fig. 14.

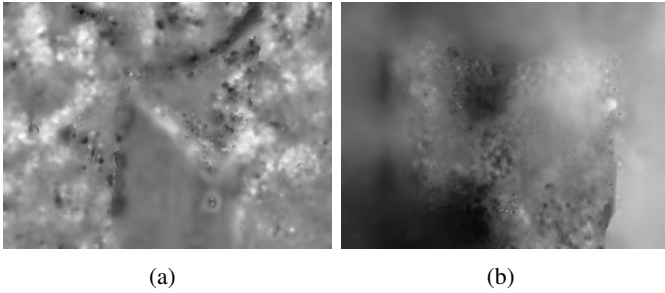


Fig. 10. Occlusion timings s for the scenes *windmill*, (a), and *corner*, (b). For non-occluded points all values for s between $s = 0$ (black) and $s = 1$ (white) are equally valid while for occluded or disoccluded points s designates the instant to switch from integration in the preceding short exposure to integration in the succeeding short exposure. Easier visual evaluation of wrong/ correct occlusion timings is possible by image interpolation, Fig. 14, 12 and 15

A. Motion Fields for Synthetic Test Scenes

We consider synthetic test scenes containing different kinds of motion. The scene *square*, Fig. 14 combines 10 pixels per time unit horizontal translational motion of the square with 15 pixels per time unit vertical motion of the background on a 225×320 image, i.e. blurred pixels at the edges of the square combine several background points as well as several foreground points. The scene *Ben*, Fig. 15, first row, contains only translational motion in front of a static background. The main challenge of this scene is the large magnitude of the motion, 14 pixels per time unit on a 300×380 pixel image, and background occlusion/disocclusion. The scene *windmill*, Fig. 15, second row, contains 7° per time unit rotational motion parallel to the image plane in front of a static background. In the *wheel* scene, Fig. 15, third row, the wheel in the background is rotating 7° per time unit while the foreground remains static. The challenge of the scene *corner*, Fig. 15, fourth row, is out-of-plane rotation of 10° around an axis parallel to the vertical image dimension, while the scene *fence*, Fig. 15, fifth row, contains translational motion of the same extent as the moving object's width.

To obtain the motion-blurred image I_B we render and average 220–500 images. The first and the last rendered image represent the short-exposed images I_1 and I_2 . Ground-truth motion is calculated from the known 3D scene motion.

To evaluate the advantage of the global optimization framework, we compare the results of the presented TV- L^1 algorithm to the results of the pointwise algorithm used in Ref. [5]. We also compare to state-of-the-art optical flow algorithms, [10], [11], [28]. For fair compar-

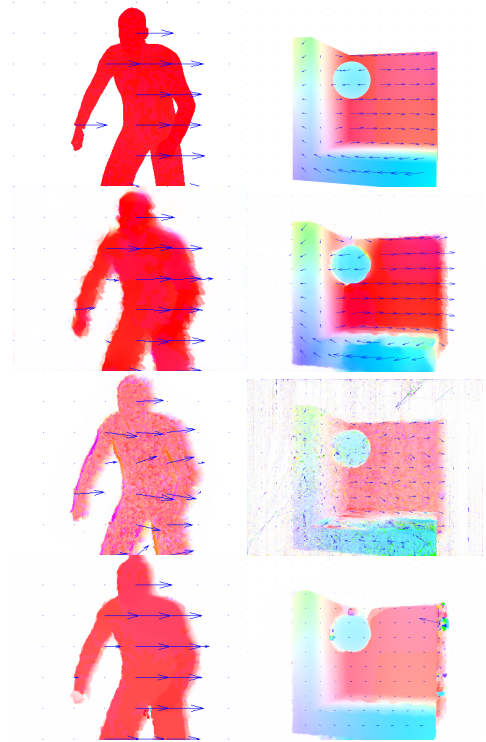


Fig. 11. Comparing motion fields for the scenes *ben* and *corner* to the ground-truth motion field (top row): While the approach of Sand and Teller [10] (second row) is prone to over-smoothing, the approach of Lim et al. [11] (third row) produces noisy motion fields. TV- L^1 regularization [28] (last row) assigns unpredictable motion to occluded points. Results of our algorithm, Fig. 15(b), profit from the TV- L^1 regularization for favoring piecewise constant motion fields and the motion blurred image for motion field assignment to occluded/disoccluded pixels.

ison, we provide the competing optical flow algorithms also with the image $I_{1.5}$, depicting the scene half way between I_1 and I_2 . We calculate the motion fields between I_1 and $I_{1.5}$ as well as between $I_{1.5}$ and I_2 . The two results are then concatenated before comparing them to the ground-truth displacement field. As optical flow works best for small displacements [11], the error of the concatenation is considerably smaller than calculating the motion field between I_1 and I_2 directly.

We choose the algorithm of Zach *et al.* [28], because it relies on the same mathematical framework as our approach. However, our method uses a long-exposed image instead of a higher frame rate of short-exposed images. We also compare to the algorithm of Sand and Teller [10] on three images, because both our method and their approach consider occlusion effects while calculating motion fields.

As our algorithm is based on signal-theoretical ideas to prevent temporal aliasing, we incorporate a comparison

to the algorithm of Lim *et al.* [11] that requires high-speed recordings as input. We simulate the high-speed camera with intermediate images such that motion between two frames is smaller than 1 pixel. Additionally we compare our earlier alternate exposure flow in Ref. [5] which is based on the same image formation model as the approach described here but applies only pointwise optimization.

As can be seen in Tab. I, our algorithm has the smallest mean angular error (MAE) for all test scenes. Also, in all test scenes, except for the rotational motion parallel to the image plane of the scenes *windmill* and *wheel*, our algorithm has the smallest mean endpoint error (MEE). The rotation within the image plane directly violates the assumption of linear motion paths in our image formation model, so here our algorithm is outperformed by TV- L^1 optical flow which does not model the motion paths in the intermediate time between the frames. In the *corner* scene with out-of-plane rotation and severe self-occlusion, our algorithm is able to produce the most accurate motion fields in angular error as well as in endpoint error. Visual comparison of the motion fields, Fig. 11 and Fig. 15(b) show, that the decrease of error is due to several reasons: The algorithm of Sand and Teller [10] tends to over-smooth motion discontinuities, Fig. 11 second row, while the algorithm of Lim *et al.* [11] returns noisy motion fields, Fig. 11 third row. The TV- L^1 algorithm [28] assigns large outlier motion vectors to occluded points, Fig. 11 last row.

B. Frame Interpolation for Synthetic Test Scenes

For evaluation of the occlusion time estimation, we interpolate intermediate images based on (9). We also interpolate intermediate frames between I_1 and $I_{1.5}$, i.e. between $t = 0$ and $t = 0.5$, using the method introduced by Baker *et al.* [29] and blending of forward and backward warping. None of the latter two methods considers occlusion. Fig. 12 gives an overview of the sum of squared differences (SSD). Note that for some images the interpolation error of our algorithm is even smaller than the SSD of ground-truth motion. This is due to the fact that inaccuracies in the motion fields can be balanced by successful handling of occlusion boundaries. The positive effect of the occlusion handling becomes also obvious when the images interpolated at $t = 0.25$ using our algorithm, Fig. 14(i) and 15(c), are compared to the corresponding images interpolated with the method of Ref. [29] and ground-truth motion, Fig. 14(g) and 15(d).

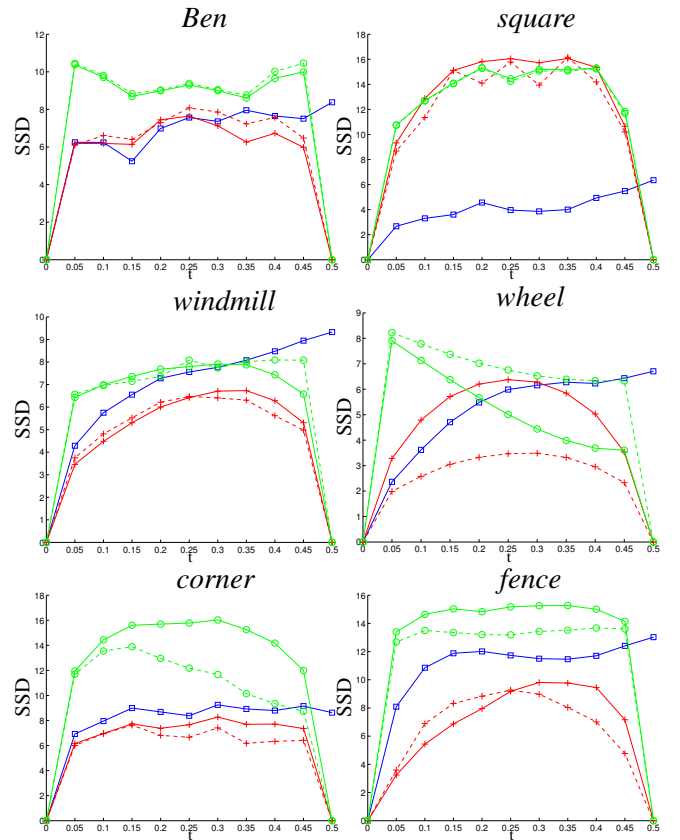


Fig. 12. The sum of squared differences (SSD) between interpolated images and ground-truth images at different instants in time. Images interpolated with our algorithm (\square) show comparable or even smaller SSD than images interpolated with forward interpolation [29] either with motion fields computed with optical flow [28] (solid, \circ) or even with ground-truth motion (solid, $+$). The same is true for forward-backward interpolation in conjunction with optical flow [28] (dashed, \circ) and with ground-truth motion (dashed, $+$).

C. Contribution of Data and Regularization Terms

In Sect. V we included the two-image color-constancy assumption (11) as an additional data term weighted by parameter γ . Setting $\gamma = 0$ results in visually convincing motion fields, Fig. 14(e), where boundaries are well defined. Incorporating the color-constancy assumption which formally only holds for non-occluded points decreases the quality of the motion fields at occlusion boundaries, Fig. 14(f). Yet the numerical error measures for flow fields such as the angular error and the endpoint error are decreased by the color constancy: for the *square* scene the mean angular error is 1.7° for $\gamma = 0.2$ and 2.55° for $\gamma = 0$ while keeping all other parameters fixed. Obviously, the motion-blurred data term (10) yields a basically correct motion field by integrating along the motion path. The additional color-constancy assumption provides subpixel accuracy [29]. The actual choice of γ

TABLE I

COMPARISON OF DIFFERENT OPTICAL FLOW METHODS FOR SIX SYNTHETIC TEST SCENES: THE MOTION FIELD COMPUTED USING TV- L^1 FOR ALTERNATE EXPOSURE IMAGES (AEI) PRESENTED IN THIS PAPER CONSISTENTLY YIELDS A SMALLER MEAN ANGULAR ERROR (MAE). THE MEAN ENDPOINT ERROR (MEE) IS COMPARABLE TO MOTION FIELDS COMPUTED WITH COMPETITIVE OPTICAL FLOW ALGORITHMS [10], [28] OR WITH ANTI-ALIASED MOTION ESTIMATION ALGORITHMS [5], [11].

	<i>Ben</i>		<i>square</i>		<i>windmill</i>		<i>wheel</i>		<i>corner</i>		<i>fence</i>	
	MAE	MEE	MAE	MEE	MAE	MEE	MAE	MEE	MAE	MEE	MAE	MEE
Sand, Teller [10]	8.42	0.91	6.48	5.72	6.78	2.95	13.39	1.27	6.40	2.85	19.12	3.36
Zach <i>et al.</i> [28]	5.81	0.59	2.25	0.62	4.87	1.69	2.59	0.60	5.05	1.27	19.44	14.75
Lim <i>et al.</i> [11]	9.01	1.46	12.19	4.88	49.63	7.69	27.29	1.82	38.40	7.73	34.17	5.23
AEI, pointwise [5]	6.31	0.99	6.52	1.79	8.64	5.47	4.19	1.02	12.87	6.30	34.41	12.64
AEI, TV- L^1	4.27	0.57	1.70	0.52	4.56	2.16	2.21	0.61	4.57	0.92	12.97	2.62

has been found to have only a small influence on the mean angular error, Fig. 13.

The parameter β weighs the smoothness of the occlusion timings in (13). We can assume the occlusion times to be locally correlated, so we regularize them. For comparison, we calculated motion fields with only pointwise evaluation of the occlusion timings, i.e. $\beta = 0$. The interpolated image for $t = 0.25$ using the results of only the pointwise evaluation of the *square* scene is shown in Fig. 14(h) or enlarged in Fig. 14(k): some pixels at the occlusion boundaries are assigned wrong timings, resulting in foreground pixels when they should show background pixels. Apart from these visual artifacts, the mean angular error of the motion field with only pointwise occlusion evaluation is increased to 2.05° . The assumption of correlated occlusion timings obviously encourages the algorithm to find more consistent motion fields which is advantageous in most real-world scenarios. The actual value of $\beta > 0$ has only small influence on overall performance, Fig. 13. Similar results are obtained for other test-scenes.

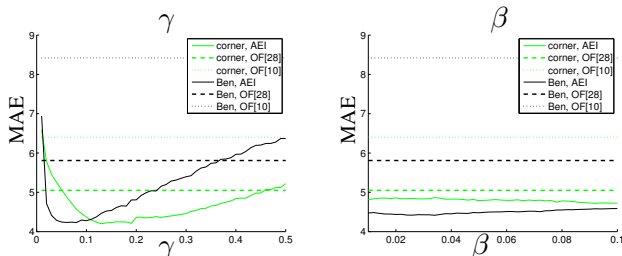


Fig. 13. Comparison of the mean angular error (MAE) for different parameter choices in our algorithm (AEI) to optimized errors of optical flow algorithms [10], [28]. The actual choice of the parameter γ or β while keeping the other parameter fixed has little influence on the MAE: for scenes *Ben* (bold/ black) and *corner* (light/ green) the MAE stays below optimized results of optical flow algorithms (dashed lines) for a wide interval.

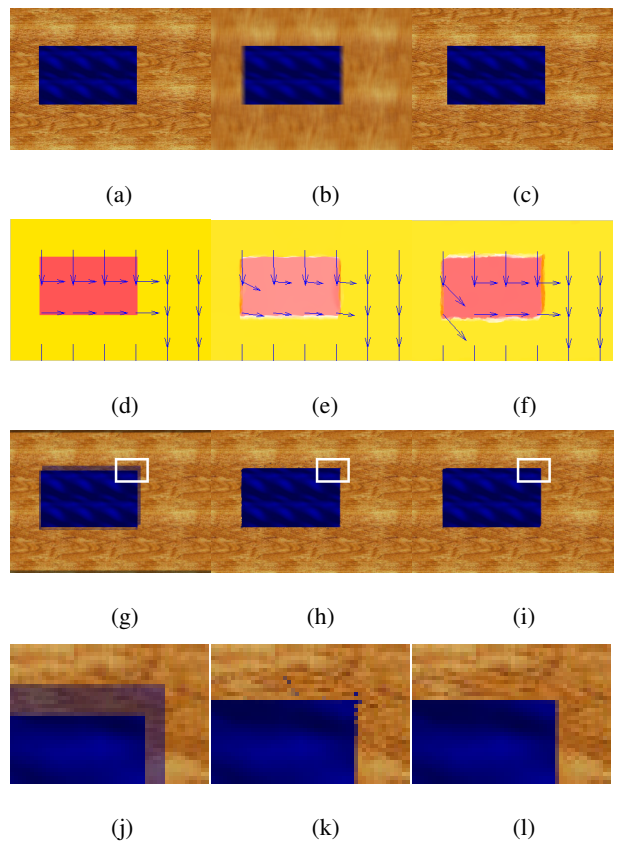


Fig. 14. The synthetic scene *square*: (a) a short-exposed, (b) a long-exposed and (c) another short-exposed image are provided as input. (d) The ground-truth motion field is compared to (e) the motion field obtained by using only the motion-blur constraint and to (f) the motion field obtained by using the motion-blur constraint plus color-constancy assumption (color coding see Fig. 9, arrow length scaled for clearer visualization). (g) Images interpolated ($t = 0.25$) with ground-truth motion fields but without occlusion timings show artifacts at occlusion borders, as (j) the enlargement of the white box shows. (h) Artifacts are reduced by interpolation with pointwise evaluated occlusion timings, see enlargement (k), and practically vanish for (i) interpolation with regularized occlusion timings, enlargement (l).

D. Real-World Recordings

We also test our method on real-world recordings. We use the built-in HDR mode of a PointGrey Flea2 camera to alter exposure time and gain between successive frames. By adjusting the gain, we ensure that corresponding pixels of static regions in the short-exposed and long-exposed images are approximately of the same intensity. With the HDR mode we are able to acquire I_1 , I_B and I_2 with a minimal time gap between the images. The remaining gap is due to the fixed 30 fps camera frame rate and the readout time of the sensor. The recorded images and the estimated motion fields are shown in Fig. 16. The scenes *juggling*, *walking*, *model train 1*, *model train 2* and *tracking*, Fig. 16 first to fifth row, are all recorded with 6.02 ms exposure time for I_1 , a 27.31 ms gap between I_1 and I_B , 39.65 ms exposure time for I_B followed by a gap of 0.48 ms and the recording of I_2 with an exposure time of 6.02 ms. For the *waving* scene, Fig. 16, sixth row, we use exposure times of 20.71 ms for I_1 and I_2 and 124.27 ms exposure time for I_B , resulting in measured gaps of 12.45 ms between I_1 and I_B and 0.48 ms between I_B and I_2 .

The *juggling* scene demonstrates vividly the advantages of using short and long exposures: the motion is very fast and the sharp images I_1 , I_2 require short exposure times of 6.02 ms. Yet the camera can only process an image every 33.33 ms. Using only short exposures leads to long gaps of 27.31 ms of unrecorded motion between images. For our method, we replace every second short exposure image with a long exposure image, reducing the gap to 0.48 ms which is due to readout time of the sensor and other hardware constraints. I_B records scene motion during the whole exposure time and provides us with temporally anti-aliased information. Notice that one of the balls still visible in I_1 disappears in I_2 , making standard optical flow computations unfeasible, but the motion-blurred image captures the path taken by the ball and enables correct motion field estimation. For this reason, our method can even handle the small ball leaving the picture.

In the *walking* scene a person walks by on a street and the leg moves on the order of magnitude of its width while her right arm is half occluded by the body. Our algorithms handles both difficulties correctly.

The scenes *model train 1* and *2* contain moving shadows and the highlights on the last wagon that are handled robustly by our algorithm.

For the *tracking* scene, the camera follows the motion of a walking person so that objects in the background

experience large displacements while the foreground remains comparatively static. Notice how even the person's black backpack is assigned the appropriate foreground motion, though it is hardly visible in front of the dark background.

In the *waving* scene, the algorithm is capable of dealing with disoccluded texture where the hand uncovers the face.

VII. LIMITATIONS AND DISCUSSION

Motion field estimation from alternate exposure images shares some of the limitations inherent to all optical flow methods. Like in all purely image-based methods, motion in poorly textured regions cannot be detected uniquely. This can be seen in the black background of the *waving* scene, Fig. 16.

Also common to all optical flow methods, we assume that motion is the only source of change in brightness, disregarding highly reflecting and transparent surfaces from the calculations.

Further we made the assumption, common in optical flow estimation, that the short exposures are free of motion blur. Practically this is regarded as satisfied if motion during the short exposure time is smaller than half a pixel.

Image noise also is a common problem and considered in the use of a suitable norm for the data-term and the regularization. While the gain and therefore the noise level in the short exposures of the alternate exposure images is increased in comparison to optimal short exposures, our algorithm does not compare single pixel values but integrates over several pixels so that noise with zero mean can cancel out.

In contrast to most optical flow methods, we are able to include occlusion explicitly into our image formation model. Arbitrarily large occlusion as well as disocclusions can be handled under the assumption that a scene-point changes its state of visibility only once. This assumption on the visibility state infers an object dependent limit on the maximal translation, as e.g. for a static background point an occluding object can move at most as far as its width before the background point reappears.

As a further difference, our image formation model works with motion paths instead of displacement fields. While motion paths can theoretically have arbitrary forms, the assumption that they are linear allows to convert from motion paths to displacement vectors by warping. Actually, linear motion paths imply that the displacement of all pixels on the path is uniform and of

constant speed. But as motion paths are allowed to vary for neighboring pixels, the approach can successfully handle also much more complex motions.

Finally, while recording the alternate exposure sequence, we replace one short exposure with a long exposure. To show the sequence to a viewer uninterested in motion detection, the long exposed frame may simply be skipped, or, to ensure a sufficient frame rate, intermediate images can be easily and quite faithfully interpolated with the proposed method.

VIII. CONCLUSION AND FUTURE WORK

In this work, we have proposed a variational approach to optical flow from a set of alternately exposed images. We refine the optimization of a general image formation model that is able to handle occlusions, large displacements and objects moving out of the image. Based on the image formation model, we derive a TV- L^1 energy functional which we solve with an efficient dual method. Our experiments show that making use of a long-exposed image improves the accuracy of the motion field calculation: the mean angular error and the mean endpoint error are reduced, not only for linear motion but also for rotational types of motion. So far, we model changes in illumination only implicitly by the robust L^1 norm, but we hope to incorporate changing illumination into future motion-blurred image formation models. In future work, we also want to apply the optimization method to non-linear motion paths which promises to be even more favorable for frame interpolation.

APPENDIX FOURIER TRANSFORM OF THE TEMPORAL DERIVATIVE

With the notations of Sect. III and assuming $u, v \neq 0$ the Fourier transform of the temporal intensity function $\phi(t) = f(x_0, y_0, t)$ is

$$\begin{aligned}\Phi(\tau) &= \int e^{-2\pi i \tau t} \phi(t) dt \\ &= \int e^{-2\pi i \tau t} f_0(x_0 - tu, y_0 - tv) dt \\ &= \iint \delta(y - (y_0 - tv)) e^{-2\pi i \tau t} f_0(x_0 - tu, y) dy dt \\ &= \iiint e^{-2\pi i (\eta(y - y_0 + tv) + \tau t)} f_0(x_0 - tu, y) dy dt d\eta.\end{aligned}$$

Substituting $x = x_0 - tu \Leftrightarrow t = \frac{x_0 - x}{u}$ for $u \neq 0$ gives

$$\begin{aligned}\Phi(\tau) &= \frac{-1}{|u|} \iiint e^{-2\pi i (\eta(y + \frac{x_0 - x}{u} v - y_0) + \tau \frac{x_0 - x}{u})} \\ &\quad f_0(x, y) dy dx d\eta \\ &= \frac{-1}{|u|} \iiint e^{-2\pi i (\eta y + \xi x)} e^{2\pi i (\eta y_0 + \xi x_0)} \\ &\quad \delta(\xi + \frac{\tau + \eta v}{u}) f_0(x, y) dy dx d\eta d\xi \\ &= - \iint e^{2\pi i (\eta y_0 + \xi x_0)} \\ &\quad \delta(\tau + \xi u + \eta v) F_0(\xi, \eta) d\xi d\eta \\ &= - \iint e^{2\pi i (\eta y_0 + \xi x_0)} F(\xi, \eta, \tau) d\xi d\eta\end{aligned}$$

ACKNOWLEDGMENT

The authors gratefully acknowledge funding by the German Science Foundation from project DFG MA2555/4-1.

REFERENCES

- [1] W. Christmas, "Filtering requirements for gradient-based optical flow measurement," *IEEE T-IP*, vol. 9, pp. 1817–1820, Oct 2000.
- [2] T. Brox, A. Bruhn, N. Papenberger, and J. Weickert, "High accuracy optical flow estimation based on a theory for warping," in *Proc. ECCV*, 2004, pp. 25–36.
- [3] L. Alvarez, R. Deriche, T. Papadopoulou, and J. Sanchez, "Symmetrical dense optical flow estimation with occlusions detection," *IJCV*, vol. 75, no. 3, pp. 371–385, 2007.
- [4] J. Xiao, H. Cheng, H. Sawhney, C. Rao, and M. Isnardi, "Bilateral filtering-based optical flow estimation with occlusion detection," in *Proc ECCV*, 2006, pp. 211–224.
- [5] A. Sellent, M. Eisemann, and M. Magnor, "Motion Field and Occlusion Time Estimation via Alternate Exposure Flow," in *IEEE International Conference on Computational Photography*. IEEE, April 2009.
- [6] A. Sellent, M. Eisemann, B. Goldlücke, T. Pock, D. Cremers, and M. Magnor, "Variational Optical Flow from Alternate Exposure Images," in *Proceedings of VMV 2009*, November 2009, pp. 135–143.
- [7] J. Aggarwal and N. Nandhakumar, "On the computation of motion from sequences of images - a review," in *Proc of the IEEE*, vol. 76, no. 8, 1988, pp. 917–935.
- [8] J. Barron, D. Fleet, and S. Beauchemin, "Performance of optical flow techniques," *IJCV*, vol. 12, no. 1, pp. 43–77, 1994.
- [9] A. Mitiche and P. Bouthemy, "Computation and analysis of image motion: A synopsis of current problems and methods," *IJCV*, vol. 19, no. 1, pp. 29–55, 1996.
- [10] P. Sand and S. Teller, "Particle video: Long-range motion estimation using point trajectories," *IJCV*, vol. 80, no. 1, pp. 72–91, 2008.
- [11] S. Lim, J. Apostolopoulos, and A. Gamal, "Optical flow estimation using temporally oversampled video," *IEEE T-IP*, vol. 14, no. 8, pp. 1074–1087, 2005.
- [12] D. Mahajan, F. Huang, W. Matusik, R. Ramamoorthi, and P. Belhumeur, "Moving gradients: a path-based method for plausible image interpolation," *ACM Trans. Graph.*, vol. 28, no. 3, p. 42, 2009.
- [13] I. M. Rekleitis, "Optical flow recognition from the power spectrum of a single blurred image," in *Proc ICIP*, 1996, pp. 791–794.

- [14] T. Pao and M. Kuo, "Estimation of the point spread function of a motion-blurred object from autocorrelation," in *Proc of SPIE*, vol. 2501, 2003.
- [15] S. Dai and Y. Wu, "Motion from blur," in *Proc CVPR*, 2008, pp. 1–8.
- [16] R. Fergus, B. Singh, A. Hertzmann, S. Roweis, and W. Freeman, "Removing camera shake from a single photograph," in *SIGGRAPH*, 2006, pp. 787–794.
- [17] J. Jia, "Single image motion deblurring using transparency," in *Proc CVPR*, 2007, pp. 1–8.
- [18] D. Kundur and D. Hatzinakos, "Blind image deconvolution," *IEEE Signal Process Mag*, vol. 13, no. 3, pp. 43–64, 1996.
- [19] A. Levin, "Blind motion deblurring using image statistics," *Adv Neural Inform Process Syst*, vol. 19, pp. 841–848, 2007.
- [20] L. Yuan, J. Sun, L. Quan, and H.-Y. Shum, "Image deblurring with blurred/noisy image pairs," in *SIGGRAPH*, no. 3, 2007.
- [21] M. Ben-Ezra and S. K. Nayar, "Motion deblurring using hybrid imaging," in *Proc CVPR*, 2003, pp. 657–664.
- [22] Y. Tai, H. Du, M. Brown, and S. Lin, "Image/video deblurring using a hybrid camera," in *Proc CVPR*, 2008, pp. 1–8.
- [23] W.-G. Chen, N. Nandhakumar, and W. N. Martin, "Image motion estimation from motion smear—a new computational model," *IEEE T-PAMI*, vol. 18, no. 4, Apr. 1996.
- [24] —, "Estimating image motion from smear: a sensor system and extensions," in *Proc ICIP*, 1995, pp. 199–202.
- [25] L. Bar, B. Berkels, M. Rumpf, and G. Sapiro, "A variational framework for simultaneous motion estimation and restoration of motion-blurred video," in *Proc ICCV*, 2007, pp. 1–8.
- [26] A. Agrawal, Y. Xu, and R. Raskar, "Invertible motion blur in video," *ACM Trans. Graph.*, vol. 28, no. 3, pp. 1–8, 2009.
- [27] P. Favaro and S. Soatto, "A variational approach to scene reconstruction and image segmentation from motion-blur cues," in *Proc CVPR*, 2004.
- [28] C. Zach, T. Pock, and H. Bischof, "A duality based approach for realtime TV- L^1 optical flow," in *Pattern Recognition*, vol. 4713, 2007, pp. 214–223.
- [29] S. Baker, D. Scharstein, J. Lewis, S. Roth, M. Black, and R. Szeliski, "A Database and Evaluation Methodology for Optical Flow," in *Proc ICCV*, 2007.
- [30] A. Chambolle, "An algorithm for total variation minimization and applications," *J Math Imag Vis*, vol. 20, no. 1, pp. 89–97, 2004.

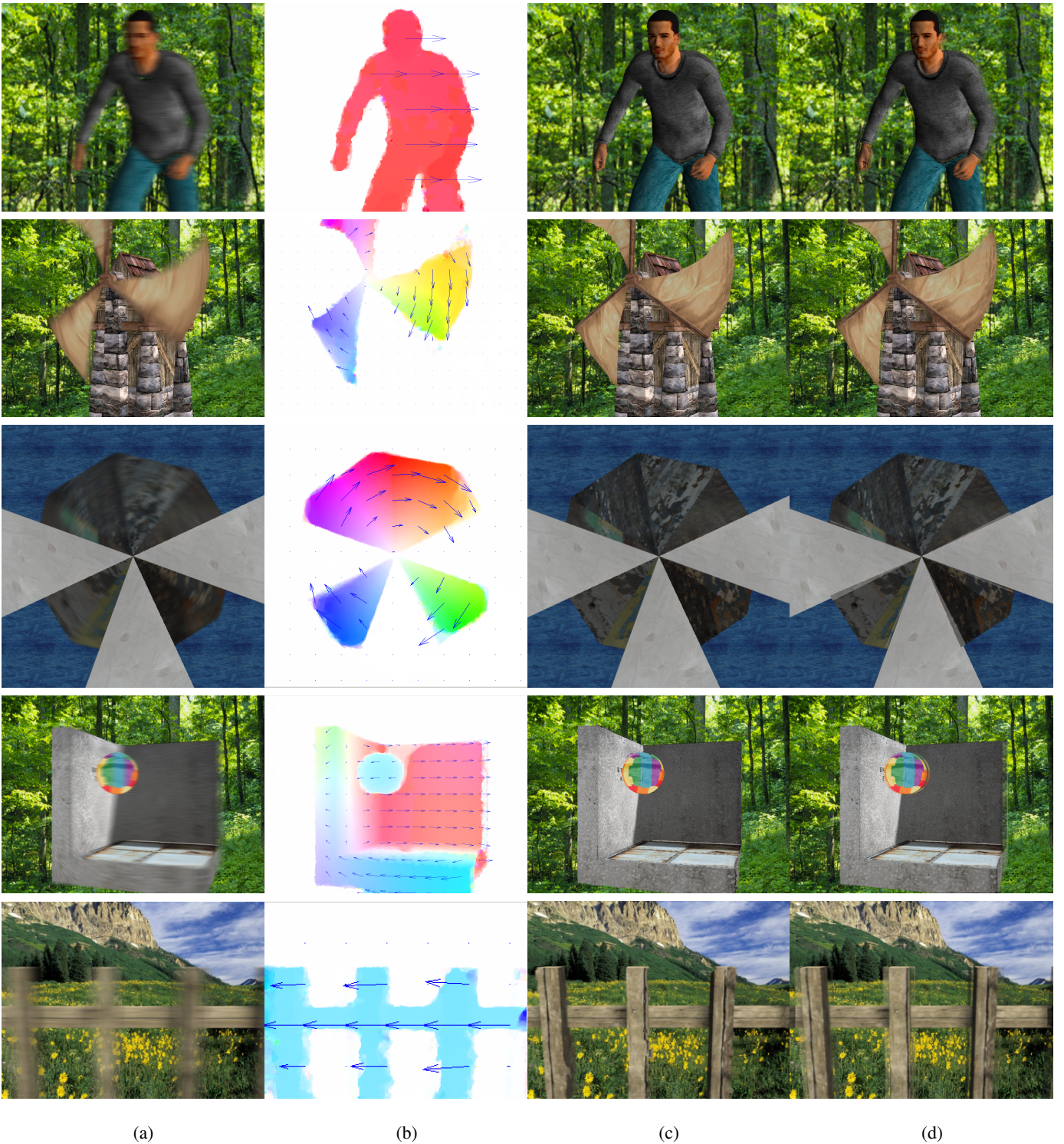


Fig. 15. Results for the synthetic test scenes (from top to bottom) *Ben*, *windmill*, *wheel*, *corner*, *fence*: (a) the motion blurred image, (b) motion fields calculated with our algorithm (directions color coded, see Fig. 9), (c) images interpolated at $t = 0.25$ with our motion paths using Eq. (9). Note that the occlusion time provided by our algorithm yields well defined occlusion borders. (d) For comparison, images interpolated at $t = 0.25$ with ground-truth displacement fields but without occlusion timings using the method described in [29] show artifacts at occlusion borders.

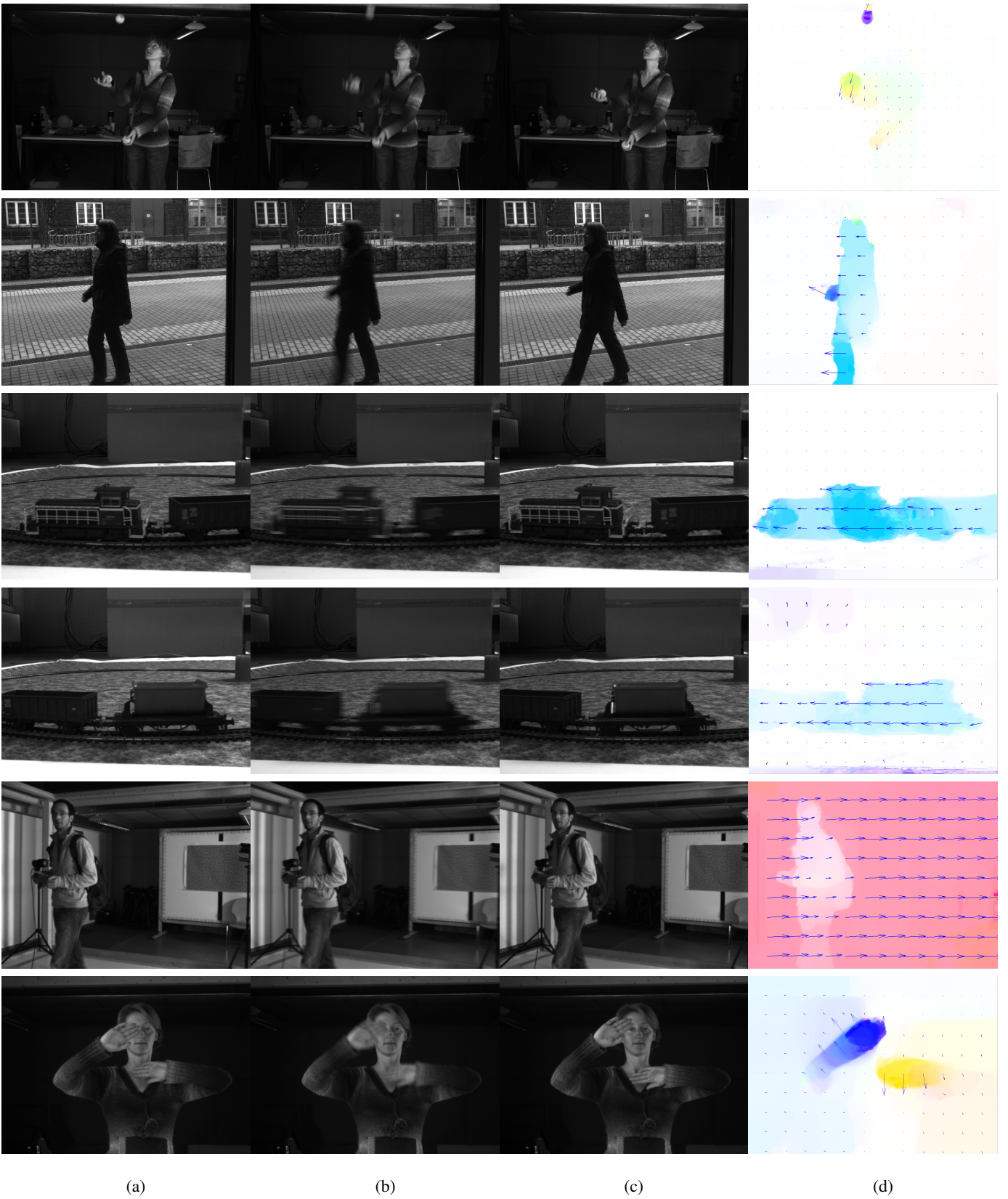


Fig. 16. The built-in HDR mode of our PointGrey camera alters exposure time and gain between succeeding frames so that (a) short, (b) long, and (c) short exposures can be acquired at comparable brightness and with minimal temporal gap between frames. (d) Reconstructed motion fields for the real-world scenes (from top to bottom) *juggling*, *walking*, *model train 1*, *model train 2*, *tracking* and *waving*.